Journal of Materials Chemistry A

ROYAL SOCIETY OF CHEMISTRY

PAPER

View Article Online
View Journal | View Issue

Cite this: J. Mater. Chem. A, 2025, 13, 31304

A chicken egg white-based amyloid–graphitic carbon nitride composite-incorporated hollow fiber membrane for efficient removal of dyes and heavy metal ions present in water†

Sooraj S. Nayak,[a] Arun M. Isloor *[a] and Ahmad Fauzi Ismail[b]

Severe water pollution due to excessive industrialization is resulting in a pure water crisis for humans and other living beings. This growing crisis emphasizes the urgent need for advanced and efficient water purification technologies to mitigate pollution and ensure the availability of pure water. To address this issue, the current study focuses on the synthesis of a chicken egg white amyloid–graphitic carbon nitride composite (AM–CN) using graphitic carbon nitride (g-C_3N_4) and egg whites through environment friendly and simple techniques. These composites were further characterized using different analytical techniques such as BET, FTIR, XRD, SEM, and TEM to understand the structure of the composite. Furthermore, these composites were embedded into hollow fiber membranes, and later, these membranes were analyzed through AFM, SEM, and hydrophilicity studies to understand the character and structure of the membrane. The filtration performance of the membrane revealed that the membrane with the AM–CN composite demonstrated enhanced performance in both pure water permeability and pollutant removal capacity. Among the fabricated membranes, the neat membrane exhibited a pure water permeability of 81 L m^{-2} h^{-1} bar^{-1}. In contrast, the highest permeability of 203 L m^{-2} h^{-1} bar^{-1} was exhibited by the M II membrane, therefore considering it as an optimized membrane. This optimized membrane also displayed the highest pollutant removal capacity of >99% for Congo red dye, >98% for Reactive black 5 and 88% for Reactive orange 16 dye. In the case of heavy metal ion removal, the same membrane displayed an impressive 99% removal of lead ions and 75% removal of mercury ions in the presence of humic acid.

Received 7th April 2025
Accepted 14th July 2025

DOI: 10.1039/d5ta02761f

rsc.li/materials-a

1. Introduction

Rapid growth of the population has increased the demand for pure water, both for drinking and other daily essential activities. Simultaneously, along with the population, the textile industry has grown to meet the demands of the increasing population. However, the expanding textile industry has also increased water pollution, mainly due to the discharge of untreated dye wastewater into natural water sources. These dye effluents contain complex organic molecules that are non-biodegradable and chemically stable for a longer period of time. This damages the aquatic ecosystem, making the water unsuitable for sustaining aquatic life forms and unfit for drinking.[1–3] Along with dyes, heavy metals such as lead, mercury, cadmium, and arsenic also pose a grave threat to water sources by contaminating both groundwater and surface water due to anthropogenic activities such as mining and industrial effluent discharge. In certain instances, geological activities also release toxic heavy metals into water reservoirs, making them unfit for usage.[4,5] This polluted water, when consumed over a period of time, leads to serious health concerns such as mutagenic and carcinogenic effects along with the destruction of biodiversity and aquatic ecosystems.[6,7] With the rise of water contamination, the development of efficient and sustainable technology to purify the water is a critical concern.

Among the various water purification technologies, membrane-based water purification has emerged as one of the most efficient and feasible technologies. Conventional water purification methods such as adsorption and coagulation have limitations in removing a mixture of heavy metals and organic dyes. Membrane technology, in contrast, provides excellent efficiency and selectivity along with scalability, making it an ideal candidate for modern water purification applications.[8–10] Across membrane technology, hollow fiber membranes excel due to their high surface area-to-volume ratio, rigid structure, and

[a]Membrane and Separation Technology Laboratory, Department of Chemistry, National Institute of Technology Karnataka, Surathkal, Mangalore, Karnataka-575025, India. E-mail: isloor@yahoo.com; isloor@nitk.ac.in; Fax: +0824-2474033; Tel: +91 9448523990; +0824-2474046, ext. 3206

[b]Advanced Membrane Technology Research Center (AMTEC), Universiti Teknologi Malaysia, Skudai, Johor Bahru 81310, Malaysia

† Electronic supplementary information (ESI) available. See DOI: https://doi.org/10.1039/d5ta02761f

enhanced performance. These membranes are superior to flat-sheet and spiral-wound membranes in terms of water flux and pollutant removal. Additionally, these membrane can operate under lower pressure conditions, reducing energy consumption and being an economically and environmentally sustainable option for large-scale water purification.[11,12] Even with these advantages, the performance of the polymeric hollow fiber membrane is affected by issues such as membrane fouling, inferior mechanical strength, and low flux due to the hydrophobicity of the polymer. To address these challenges, mixed matrix hollow fiber membranes (MMHFMs) are studied for their advantages over polymeric hollow fiber membranes. In MMHFMs, nanomaterials or functional composites are incorporated into the hollow fiber membrane matrix, thereby enhancing the overall membrane performance.[13,14] Nanomaterials such as metal oxide nanoparticles, graphene oxides, carbon nitrides, and metal–organic frameworks (MOFs), when incorporated into membranes, they have improved membrane hydrophilicity, leading to enhanced water flux and improved antifouling properties.[15–17] Additionally, these materials have also enhanced the rejection efficiency of dyes and heavy metal ions, offering an effective and efficient toward water purification.

Across different functional materials, amyloid protein-based composites have gained significant attention in the past few years for their potential application in water treatment, mainly in adsorption and membrane-based filtration processes.[18,19] Amyloid proteins are basically misfolded proteins and offer several properties that can be manipulated and modified to give the required characteristics. These protein materials are known for possessing good mechanical properties, enhanced surface area, and biocompatibility, and can be easily sourced from plants and animals. Amyloid proteins or their composites, when used in membrane-based water treatment applications, have enhanced the performance of the filtration system. A study demonstrated the development of a hybrid membrane consisting of activated carbon and amyloid fibrils that effectively removed environmental pollutants and heavy metals. The membrane also displayed a minimal reduction in performance and comparable efficiency for multiple cycles of wastewater purification.[20] Bolishetty and group members demonstrated the highly efficient removal of diverse clinically relevant radioactive compounds from hospital wastewater using the same activated carbon and amyloid fibril hybrid membrane. The membrane has been reported to remove 99.8% of radionuclides, namely technetium (Tc-99), iodine (I-123), and gallium (Ga-68), by a single-step filtration process.[21]

Another study reported that an amyloid fibril-based hybrid membrane is effectively capable in removal of per- and polyfluoroalkyl substances (PFASs) from water sources with a removal capacity of 96% from real water samples. These carbon–amyloid hybrid membranes exhibited excellent absorption capability to absorb long-chain PFASs.[22] Peydayesh and coworkers synthesized amyloid fibril-based aerogel sourced from lactoglobulin for the removal of organic pollutants through adsorption studies. Pollutants such as Bentazone, Ibuprofen, and Bisphenol A were used as model pollutants under quasi-static conditions in the absence of pressure. The aerogel displayed excellent pollutant removal efficiencies of 92%, 78%, and 98% for Bentazone, Bisphenol A, and Ibuprofen, respectively. Regeneration of the aerogels was also carried out for 3 consecutive cycles, exhibiting reusability without any changes in pollutant removal capacity.[23] In a recent study, Yang and team members synthesized plant-derived amyloid fibrils sourced from wheat flour with a simple, scalable method and tested it as an absorbent for the removal of organic dyes Eosin Y and Congo red. The fibrils exhibited good adsorption capacities of 333 mg g^{-1} and 138 mg g^{-1} for CR and EY, following the Langmuir adsorption isotherm, demonstrating the potential of amyloid protein towards water treatment.[24] Although several studies have been carried out on the use of amyloid-based materials for water treatment, the majority of the studies are focused on adsorption-based processes instead of continuous filtration systems. Moreover, the amyloid-incorporated membranes reported in the literature are not free-standing membranes, which limits their applicability in long-term filtration systems. This limitation hinders their practical usage towards durable and scalable water purification technologies.

In the current study, we addressed the above limitations by developing a novel free-standing hollow fiber membrane incorporated with a carbon nitride–amyloid composite for water purification. Unlike most reported amyloid-based composites that incorporate metal oxides or metal-containing components, the composite developed in this study is entirely metal-free, representing an advancement in sustainable membrane materials. The synthetic process involved is environmentally benign and economically viable without the use of any harsh chemicals and complex synthetic methods. The composite is made of low-cost graphitic carbon nitride encapsulated within the amyloid protein matrix. In this structure, the carbon nitride provides mechanical support to the soft amyloid structure, resulting in a mechanically stable yet flexible composite. This design improves the structural integrity of the membrane along with enhancing long-term water filtration performance, making it a promising candidate for practical water treatment applications.

2. Materials and methods

Polysulfone (PSf) was acquired from Solvay. Choline chloride, polyvinyl pyrrolidone (K-30), melamine, *N*-methyl pyrrolidone (NMP) and lead(II) nitrate were procured from Loba Chemie. Mercury(II) chloride, Congo red, Reactive orange 16 and Reactive black 5 were obtained from Sigma Aldrich. Humic acid and bovine serum albumin (BSA) were purchased from Highmedia. *p*-Toulenesulfonic acid (PTSA) was sourced from TCI Chemicals, and chicken eggs were procured from a local supermarket in Mangalore.

2.1. Synthesis of the amyloid–carbon nitride (AM–CN) composite

In the current study, bulk carbon nitrides were initially synthesized using a procedure from a previous article.[25] To obtain thermally exfoliated carbon nitrides (g-C_3N_4), 2 grams of

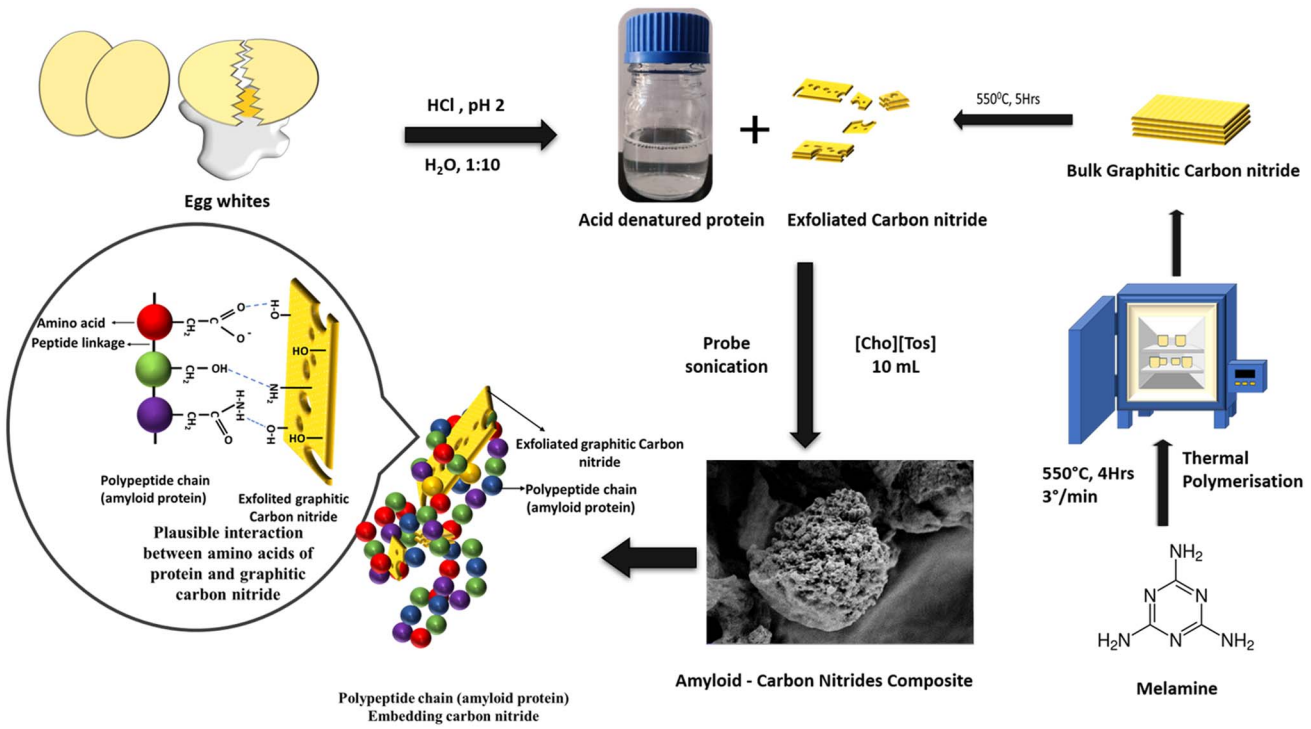

Fig. 1 Synthesis of an amyloid–carbon nitride (AM–CN) composite.

bulk carbon nitrides were placed in a silica crucible and covered with a lid. The crucible was further heated at 550 °C for 5 hours at a ramp rate of 5 °C in a muffle furnace. After cooling, the material was crushed and stored for further modification.

For the synthesis of amyloid–carbon nitride composites, initially, egg whites were separated from the whole egg, to which DI water was added in a 1 : 10 ratio. The mixture was stirred for 5 minutes (refer to Fig. 1) with a glass rod and then filtered through normal filter paper to remove fats. To the filtered solution, 2 M HCl was added until the pH reached 2; this solution is called an acid-denatured protein solution (ADPS). Subsequently, 50 ml of ADPS was taken in a beaker, and 50 mg of thermally exfoliated carbon nitrides were added and probe sonicated for 1 hour at 20 Hz frequency. Finally, to the above solution, 5 ml of 1 M deep eutectic solvent (DES) solution prepared from a 1 : 1 ratio of choline chloride and PTSA was

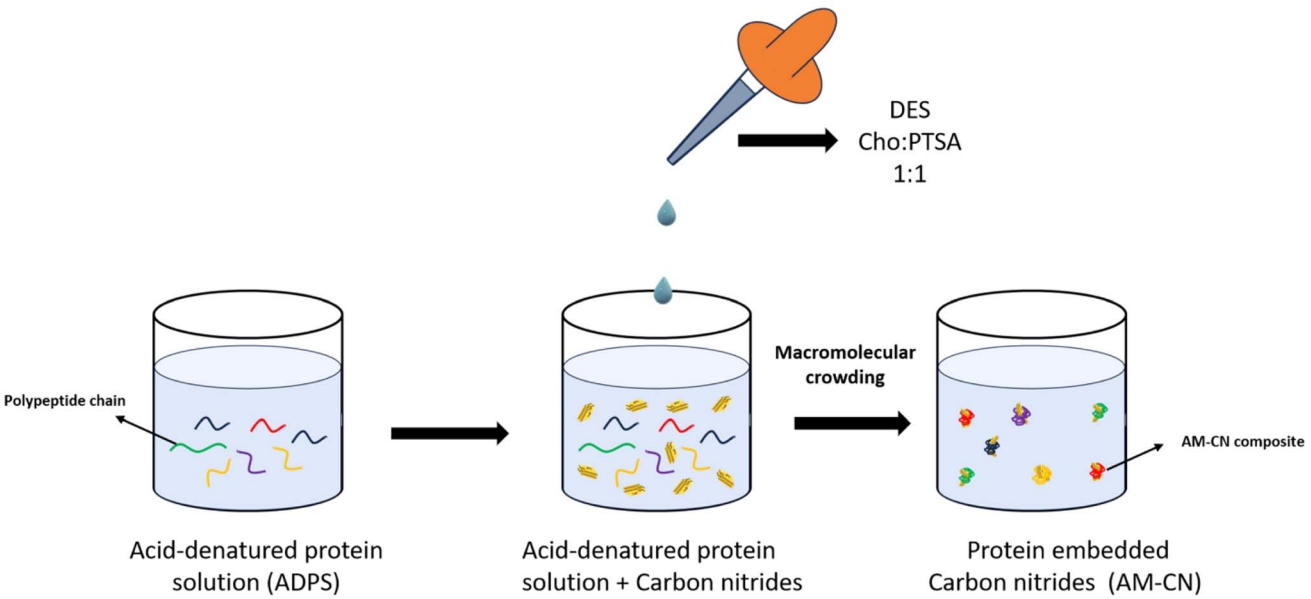

Fig. 2 Formation of an AM–CN composite through macromolecular crowding.

added with continuous stirring to obtain a white precipitate. This precipitate contained amyloid protein embedded carbon nitrides, forming a composite.

The composite formation occurs due to macromolecular crowding of proteins, which leads to their misfolding in the presence of DES (depicted in Fig. 2). During the protein precipitation process, the carbon nitrides present in the solution become entrapped within the protein chains through various interactions (H-bonding, electrostatic, and π–π interactions), leading to the formation of this composite. The resulting white precipitate was further washed with water 3 times and later lyophilized (Gold SIM-Freeze dryer FD5-2.5E) for 18 hours to obtain dried composite powder.[26]

2.2. Fabrication of hollow fiber membranes

Hollow fiber membranes incorporated with amyloid–carbon nitride composites were fabricated *via* the dry-wet spinning method employing a phase inversion process. First, the polymer solution (dope solution) was prepared based on the formulation given in Tables 1 and 2 displays the fiber spinning parameters. Initially, a certain volume of NMP solvent was taken to this a specific amount of PVP was added and sonicated for 15 minutes to dissolve the PVP in the solvent. Subsequently, a specific amount of the synthesized composite was added to the solution, followed by sonication for an hour to obtain a uniform dispersion. Furthermore, polysulfone polymer was added to the above solution and stirred for 24 hours at 60 °C to obtain a homogeneous dope solution. The dope solution is further degassed and poured into the dope reservoir of the hollow fiber spinning unit. The reservoir is pressured with nitrogen gas, and the polymer solution is made to flow through the spinneret. As soon as a few polymer droplets fell into the coagulation bath, DI water was introduced into the spinneret as the bore liquid. Shortly thereafter, a continuous stream of polymer solution, along with bore liquid, flowed into the coagulation bath, forming hollow fiber membranes. The freshly formed hollow fiber membranes were passed through a water bath and collected over the winder wheel. The collected fibers were cut into required lengths and submerged in DI water for 24 hours. Later, these membranes were immersed in a 20% glycerol solution for 48 hours, after which they were air-dried and stored until further use.[27]

Table 1 Membrane compositions

Membrane code	PSf (g)	PVP (g)	NMP (g)	AM–CN (g)
NEAT	20	1	79	0
M I	20	1	79	0.025
M II	20	1	79	0.050
M III	20	1	79	0.075

Table 2 Hollow fiber spinning parameter[a]

Parameter	Spun fiber value
Dope extrusion rate (mL min^{-1})	3
Bore extrusion rate (mL min^{-1})	5
Bore fluid	DI water
Air gap (cm)	1
Spinneret dimension (mm)	1.1/0.55 (OD/ID)

[a] ID-inner diameter, OD-outer diameter (units in millimeters).

3. Characterization

3.1. Characterization of the synthesized composite

To verify the synthesis and structural properties of the amyloid–carbon nitride composite, multiple analytical techniques were utilized. Functional analysis was confirmed through FT-IR spectroscopy, and structural analysis was carried out through the XRD technique. Particle size and zeta potential analyses were carried out to evaluate the size and surface charge of the composite. The surface area and porosity of the composite were evaluated through BET analysis. Furthermore, SEM and TEM imaging were employed to understand the morphology and structural details of the synthesized composite.

3.2. Characterization of the synthesized composite-incorporated hollow fiber membrane

To analyze the influence of the amyloid–carbon nitride composite on the structure, morphology and properties of the hollow fiber membrane, multiple characterization techniques were employed. The internal structure of the membrane was analyzed through Scanning Electron Microscopy (SEM). Atomic Force Microscopy (AFM) was employed to study the topology and surface features of the membrane. Contact angle measurements were carried out to evaluate the hydrophilicity. Additionally, membrane porosity and wettability were determined through the dry-wet weight method using theoretical calculations based on the protocols given in the literature.[28–30]

3.3. Water permeability and antifouling studies

Water permeability and antifouling properties of the fabricated hollow fiber membrane were evaluated using a custom-made cross-flow filtration setup. Initially, the dried hollow fiber membranes were cut into 15 cm lengths each, and 5 of these membranes were potted onto a hex nipple using epoxy. Once the epoxy was hardened, the potted membranes were installed in the filtration setup, and DI water was allowed to pass through the setup. In the beginning, the pressure of water flow was set to 1.5 bar for 30 minutes; this process is called compaction. After compaction, the water flow pressure was reduced to 1 bar, and at every 10-minute interval, the amount of water permeated through the membrane was collected and measured to calculate the pure water permeability of the membrane. The formula to calculate pure water permeability (J_{w1}) is given in eqn (1).

$$J_{w1} = Q/n\pi D_i t \Delta P L \quad (1)$$

where 'J_{w1}' is the pure water permeability (L m^{-2} h^{-1} bar^{-1}), 'Q' is the volume of water collected (in liter), 't' is the time interval

of water collection (in hours), 'n' is the number of hollow fibers, 'L' is the length of the hollow fiber membrane (in meters), 'D_i' is the internal diameter of hollow fiber membrane (in meters), and 'ΔP' is the transmembrane pressure (in bar).

After pure water permeability testing, the above membranes were used to evaluate their antifouling properties. A protein solution containing 800 ppm of BSA was circulated through the filtration setup at 1 bar for 80 minutes. Every 10 minutes, the permeate was collected and measured to calculate the BSA solution permeability, denoted as 'J_p'. Following this, the membranes were washed with water for 30 minutes to remove the adhered protein from the membrane surface. Subsequently, water permeability was reanalyzed using the cleaned membranes for another 80-minute duration, and this new pure water permeability is denoted as 'J_{w2}'. Using the above three permeability values, different antifouling parameters were derived, namely flux recovery ratio, reversible fouling, irreversible fouling and total fouling. The formulae to calculate these parameters are given below.[31,32]

$$\mathrm{FRR}\% = \left(\frac{J_{w2}}{J_{w1}}\right) \times 100 \quad (2)$$

$$R_r(\%) = \left(\frac{J_{w1} - J_{w2}}{J_{w1}}\right) \times 100 \quad (3)$$

$$R_{ir}(\%) = \left(\frac{J_{w2} - J_p}{J_{w1}}\right) \times 100 \quad (4)$$

$$R_t(\%) = \left(\frac{J_{w1} - J_p}{J_{w1}}\right) \times 100 \quad (5)$$

3.4. Rejection capability

To evaluate the pollutant rejection capability of the fabricated hollow fiber membranes, they were initially cut into 15 cm lengths and potted in a hex nipple using epoxy. These membranes are then compacted at 1.5 bar pressure for 30 minutes, following the same procedure as carried out in the water permeability test. Later on, the rejection is carried out at 1 bar pressure using different pollutants as feed solutions. In this study, textile dyes and heavy metal ions are used as pollutants. For dye removal studies, Congo red, Reactive black 5, and Reactive orange 16 were used at 10, 30 and 50 ppm concentrations as feed solutions. The permeate collected during rejection studies was analyzed using a UV-vis spectrometer for its absorbance value. Based on this absorbance value, the concentration of the dyes was calculated, and their rejection percentage is calculated using eqn (6).

In the case of heavy metal ion removal studies, a single solution containing 5 ppm of lead ions, 5 ppm of mercury ions and 10 ppm of humic acid was prepared and used as the feed solution. This feed solution was designed to simulate to groundwater conditions, as humic acid is usually found alongside heavy metal ions in natural groundwater sources. The permeate collected during the heavy metal ion rejection studies is analyzed using an inductively coupled plasma optical emission spectrometer (ICP-OES) instrument. Finally, using the concentration results from ICP-OES, the rejection percentage is calculated using eqn (6):

$$\text{Rejection } \% = 1 - \left(\frac{C_p}{C_f}\right) \times 100 \quad (6)$$

4. Results and discussion

4.1. Characterization of the synthesized composite

4.1.1. FT-IR analysis. FTIR spectra of bare exfoliated graphitic carbon nitride and the composite AM–CN are given in Fig. 3. The spectrum of carbon nitride displays a weak broad peak from 3500–3000 cm^{-1}, corresponding to the $-NH_2$ groups and surface hydroxyl groups. The peaks from 1600–1200 cm^{-1} correspond to the aromatic stretching of –C–N, while the peak at 800 cm^{-1} corresponds to the vibration of triazine units. Similarly, the spectrum of the composite displays a broad peak at 368 cm^{-1} linked to the amine groups and hydroxyl groups. The peaks at 2961 cm^{-1} and 2926 cm^{-1} correspond to the $-CH_2$ groups present in the protein structure, while the peaks at 1638 cm^{-1} and 1517 cm^{-1} are linked to the 1° and 2° amides of the proteins.[33,34] Finally, the peak at 814 cm^{-1} is associated with the triazine units of carbon nitride, confirming the presence of both carbon nitride and amyloid protein in the composite.

4.1.2. XRD analysis. XRD analysis of bare exfoliated carbon nitride and the composite was carried out, and their diffraction patterns are given in Fig. 4. The diffraction pattern of the bare carbon nitride shows a strong peak indexed at 27°, which

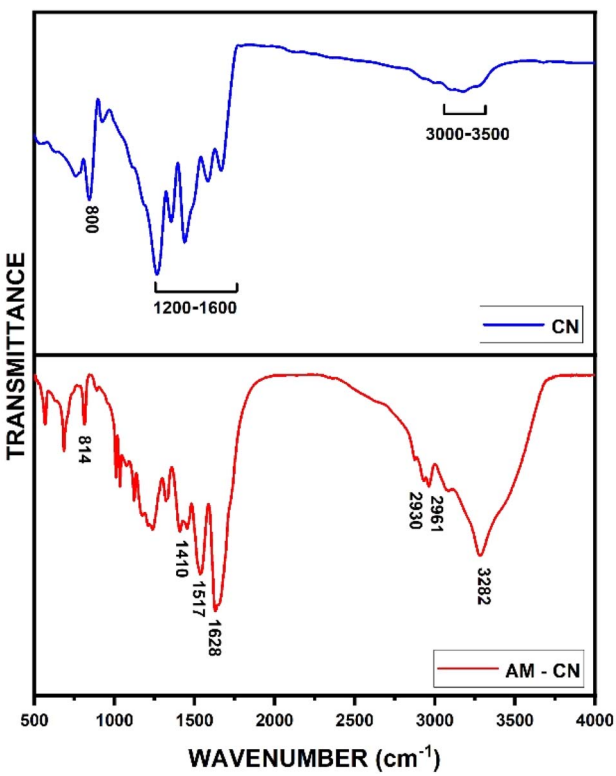

Fig. 3 FTIR spectra of graphitic carbon nitride and the AM–CN composite.

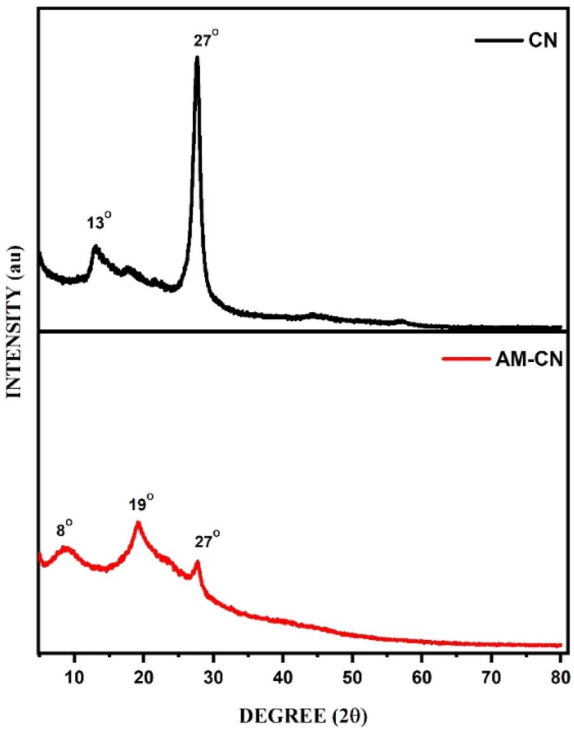

Fig. 4 X-ray diffraction patterns of graphitic carbon nitride and the AM–CN composite.

corresponds to the interlayer stacking of the aromatic conjugated system, and another peak at 13° corresponds to the in-plane structural packing of carbon nitride.[35] Similarly, the diffraction peaks of the AM–CN composite display a peak at 19° relating to the β sheet stacking between adjacent strands of the amyloids and a peak at 8° relating to the inter-sheet spacing between β sheets in the amyloids.[36,37] Additionally, the composite also displayed a peak at 27°, which is the characteristic peak of carbon nitride, confirming the presence of carbon nitride in the composite. However, the peak at 13° of the carbon nitride is overlapped in the composite, making it not visible in the diffraction pattern of the composite.

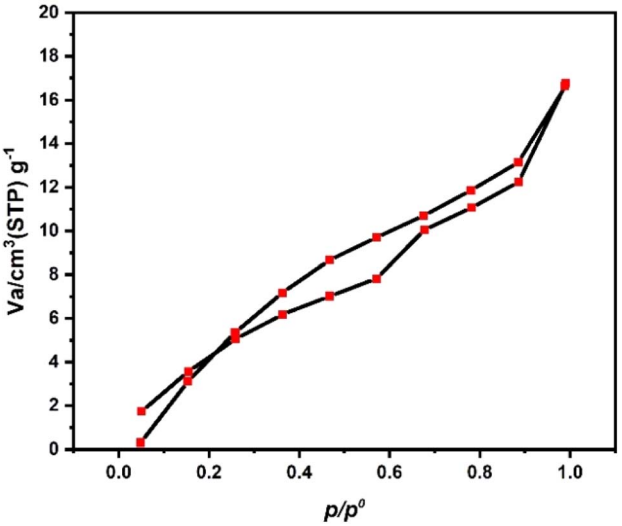

Fig. 6 Brunauer–Emmett–Teller N_2 adsorption–desorption isotherm of the AM–CN composite.

4.1.3. Particle size and zeta potential analysis. Particle size analysis of bare exfoliated graphitic carbon nitride and the AM–CN composite was carried out and is presented in Fig. 5. The analysis revealed that the exfoliated carbon nitride particle size ranged from 350–700 nm. In contrast, the composite particle size was found in the range from 200–550 nm. The slight decrease in the particle size of the composite is observed, which can be attributed to probe sonication, which facilitates delamination and breaks down carbon nitrides into smaller segments. Even after the formation of the composite, the particle size range of the composite is less than that of the bare carbon nitride, providing it with an enhanced surface area than its counterpart. Zeta potential analysis of the exfoliated carbon nitride and the AM–CN composite at neutral pH is also presented in Fig. 5. This analysis is carried out to study the surface charge of the materials. In this study, it is found that the bare carbon nitride displays a zeta potential of −17 mV, whereas the AM–CN composite displays a zeta potential of +21 mV. The shift

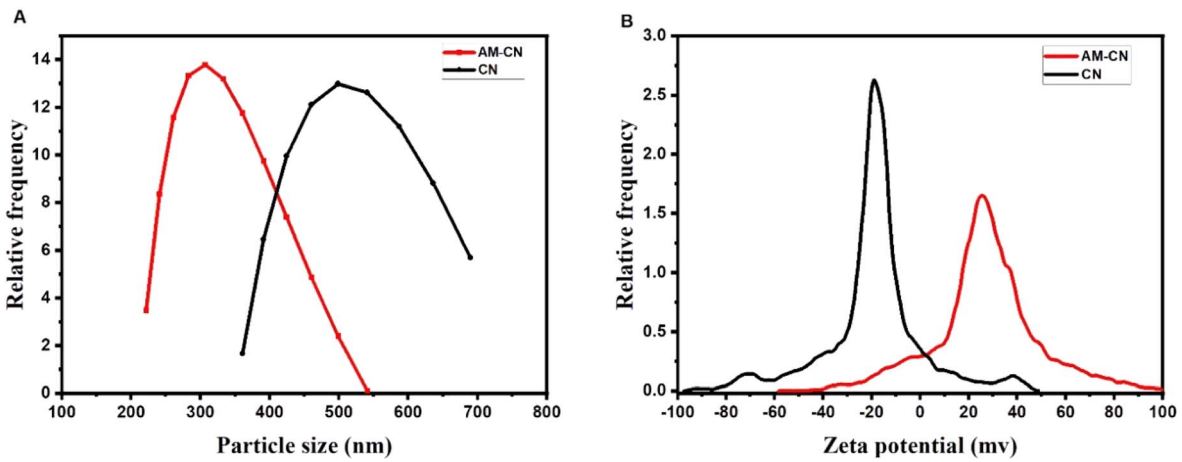

Fig. 5 (A) Particle size and (B) zeta potential of carbon nitride and the AM–CN composite.

to a positive zeta potential confirms the formation of the composite, as the synthesized amyloid is said to be positively charged.[26] Typically, proteins are known to contain both negative and positive charged species, but the net charge is determined by predominant charge-bearing groups. In the current study, positively charged species are found in abundance; hence, the composite exhibits a net positive charge.

4.1.4. BET analysis. BET analysis provides details about a material's surface area, pore volume and pore structure. The BET analysis of the AM–CN composite revealed that the composite displayed a surface area of 21.181 $m^2 g^{-1}$ with a pore volume of 0.02591 $cm^3 g^{-1}$ and an average pore radius of 24 Å. The adsorption–desorption isotherm graph of the composite is presented in Fig. 6, yielding a hysteresis loop of a type IV isotherm, which reveals the mesoporous nature of the composite.

4.1.5. SEM imaging (composite). Scanning electron microscopy of the composite provides valuable insights into the morphology or structure of the amyloid–carbon nitride composite. The SEM images of the composite are given in Fig. 7. Images display partial engulfment of the carbon nitride by the proteinaceous matrix. This structural arrangement increases the active adsorption sites of the composite. Furthermore, carbon nitride also acts as a supporting template during the folding of proteins, facilitating composite formation. The morphological features observed in SEM images were also further validated through TEM imaging.

4.1.6. TEM imaging. TEM imaging was carried out to analyze the structure of the composite or material. The TEM images of both the AM–CN composite and bare exfoliated graphitic carbon nitrides are displayed in Fig. 8(A). These images reveal that the carbon nitrides displayed delaminated layered structures, whereas the AM–CN composite displays irregular morphology. These irregular structures of the composites are formed due to the non-uniform folding of the protein into aggregates. During this process, the carbon nitrides present in the solution get engulfed by protein aggregates, resulting in a carbon nitride-embedded protein composite. The presence of embedded carbon nitrides within the composite is further confirmed in the TEM images of the composite, as displayed in Fig. 8(B).

4.2. Characterization of the synthesized composite-incorporated hollow fiber membrane

4.2.1. SEM imaging. SEM imaging was employed to study the morphology of the fabricated membranes. Cross-sectional SEM images of both neat and optimized membranes were captured to assess the influence of the AM–CN composite over the membrane. Fig. 9 presents the SEM images of both the

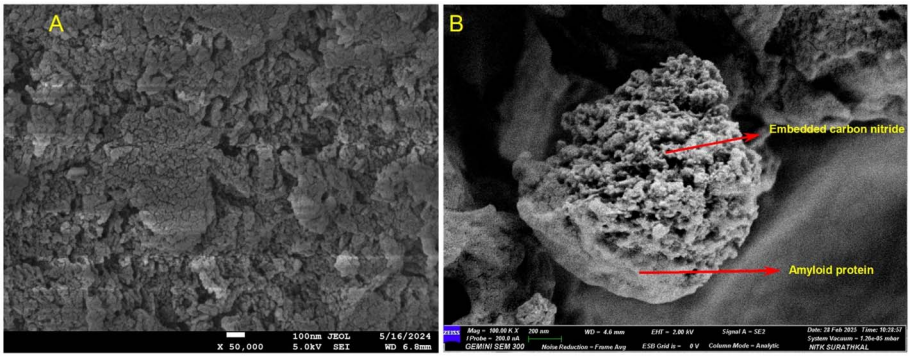

Fig. 7 SEM images of (A) carbon nitride and (B) the AM–CN composite.

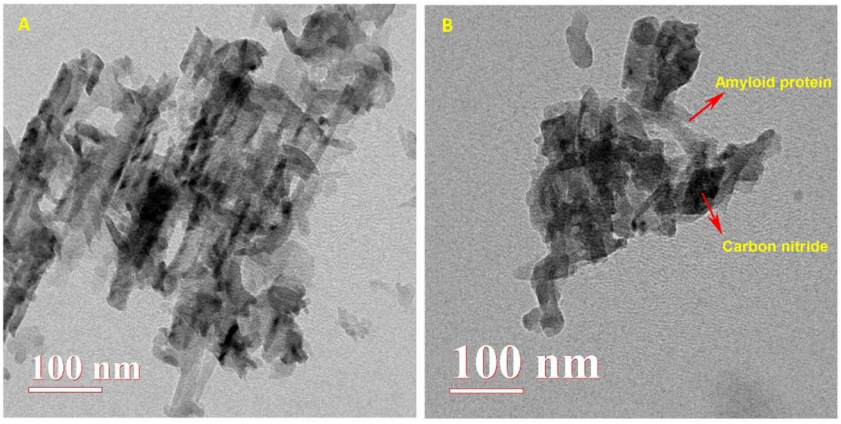

Fig. 8 TEM images of (A) carbon nitride and (B) the AM–CN composite.

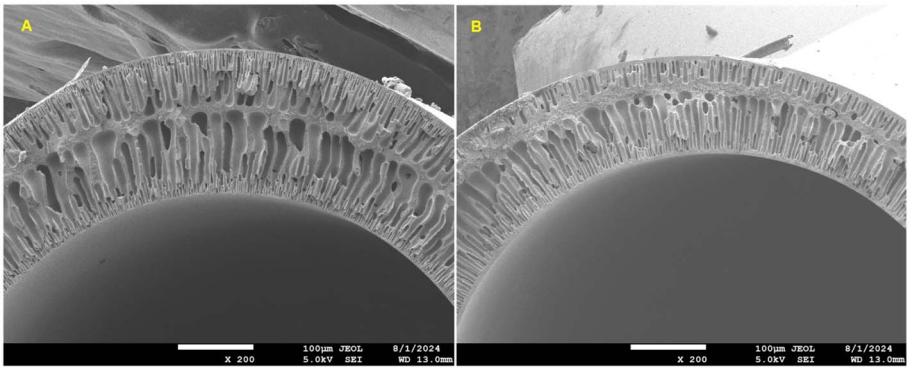

Fig. 9 Cross-sectional scanning electron microscope images of a hollow fiber displaying skin and a sub-layer: (A) neat membrane and (B) M II membrane.

Table 3 Surface parameters from AFM analysis

Membranes	Neat	M II
Surface area	429 μm^2	405 μm^2
R_a	64 nm	26.5 nm
R_q	99 nm	17.8 nm
R_{max}	1545 nm	402 nm

hollow fiber membranes. Even though both membranes displayed an asymmetric structure, the optimized membrane (M II) displayed a dense skin layer with a compact arrangement of finger-like protrusions. Furthermore, the sub-layer of the optimized membrane displayed an expanded structure with distinct macrovoids compared to the neat membrane. The presence of a dense skin layer and the expanded distinct sublayer are responsible for the higher rejection capacity and increased permeability with good mechanical support in comparison to the neat membrane. These changes in the morphology are mainly associated with the incorporation of the composites into the membrane matrix. During the phase inversion process, the solvent from the polymer solution demixes through the skin layer; while doing so, the composites tend to move towards the skin layer as they interact with the solvent, which decreases the rate of phase inversion. As a result, these composites are mostly present on the surface and skin layer of the membrane, which enables them to interact with water and pollutants more readily, leading to improved rejection capacity and water permeability.

4.2.2. AFM analysis. AFM analysis was employed to disclose the surface topology and roughness of the fabricated membrane. Both the neat polysulfone and the optimized M II membrane were analyzed. Table 3 presents the different parameters of AFM analysis, while Fig. 10 displays topological images of the analyzed membranes. The results reveal that the neat membrane exhibited a roughness of 64 nm while the M II membrane demonstrated a reduced roughness of 26.5 nm. The

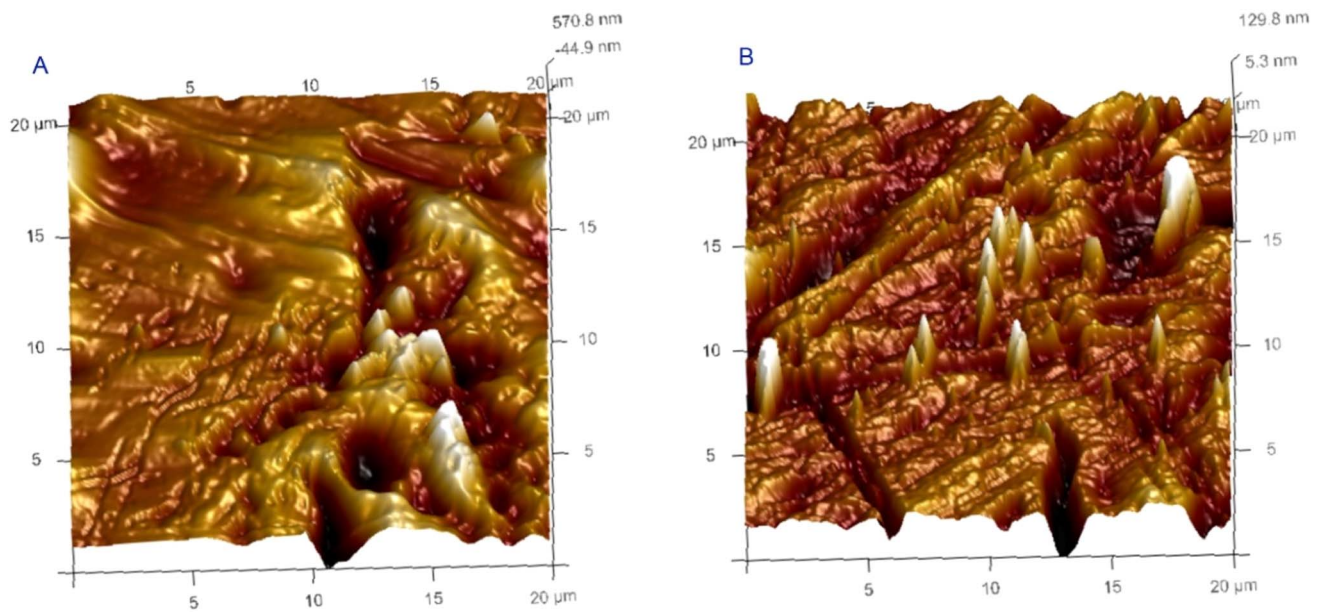

Fig. 10 AFM 3D surface topography images of (A) neat and (B) M II membranes.

reduction of roughness implies that the incorporation of the composite has led to a smoother membrane surface, mainly due to its influence during the phase inversion process. A smoother surface reduces the attachment of the foulants, thereby improving the antifouling behavior of the membrane.[38,39] The observed antifouling behavior of the optimized membrane can be correlated with the findings of antifouling studies carried out in this work.

4.2.3. Contact angle measurements. Contact angle measurement of the membranes is a fundamental parameter to analyze the membrane hydrophilicity. This analysis can also be correlated with the water permeability, as an increase in hydrophilicity enhances water permeability of the membrane. In the contact angle analysis, the membrane with a higher degree of angle is said to be hydrophobic in nature, and if the angle decreases, then the membrane is said to be of hydrophilic nature.[40] Contact angle measurements of all the fabricated membranes are given in Fig. 11. The results state that the neat membrane is hydrophobic in nature with a contact angle of 89°. However, incorporating the composite into the membrane matrix increased the hydrophilicity. This improvement is due to the presence of hydrophilic functional groups such as surface hydroxyl groups, amine groups, and amide groups within the composite. Among all the membranes, the M II membrane displayed the highest hydrophilicity. Contrary to this, the M III membrane displayed a decrease in hydrophilicity despite containing a higher amount of composite. This reduction is likely due to the aggregation of the composite during polymer solution preparation, resulting in a non-uniform dispersion. Another important factor of a membrane is the surface energy. It is defined as the ability of the membrane surface to interact with liquid molecules. A higher surface energy leads to a stronger interaction with the water molecules, subsequently enhancing membrane permeability. In the current study, the M II membrane displayed the highest surface energy, aligning with the results of permeability studies. The surface energy of the membrane is calculated using the contact angle of the membrane.[41] The surface energy of all the fabricated membranes is tabulated in Table 4.

Table 4 Porosity and surface energy of the fabricated membranes

Membrane code	Porosity	Surface energy (mN m^{-1})	Average permeability (L m^{-2} h^{-1} bar^{-1})
Neat	51	73.2	81.8
M I	66	78.2	118.7
M II	70	84.5	203.1
M III	68	80.7	163.2

4.2.4. Water uptake studies. Water uptake studies are carried out to investigate the water-holding capacity of the membrane. The hydrophilicity of the membrane can be directly correlated with the water uptake capacity, as an increase in hydrophilicity of the membrane allows the membrane to hold onto more water molecules. Similarly, porosity of the membrane can also be associated with the water uptake studies as higher porosity allows the membrane to accumulate more water within the pores, thereby increasing water uptake of the membrane. Water uptake measurements of the fabricated hollow fiber membrane are given in Fig. 12, while porosity of the membranes is tabulated in Table 4. From both studies, it can be concluded that neat membrane displays the least porosity and water uptake. However, with the incorporation of the composite, both water uptake and porosity values increase, recording the highest value of both the water uptake and porosity in the M II membrane. After this optimal composition, any further increase in the dosage results in a decline of both the parameters. This decrease can be associated with aggregation of the composites in the solution at higher dosages, resulting in blocking up of the pores and channels, thereby decreasing the water uptake capacity of the membrane.

4.2.5. Pure water permeability study. A time-dependent pure water permeability study of all the fabricated membranes

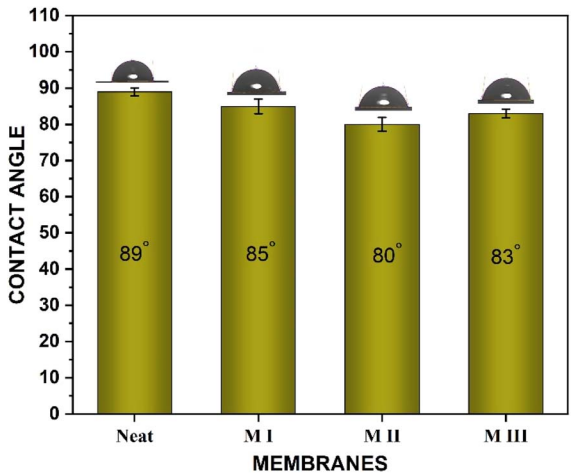

Fig. 11 Water contact angle measurements of all the fabricated hollow fiber membranes.

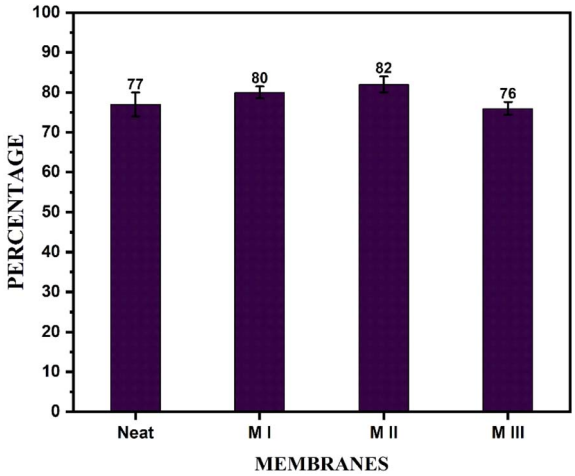

Fig. 12 Water uptake measurements of all the fabricated hollow fiber membranes.

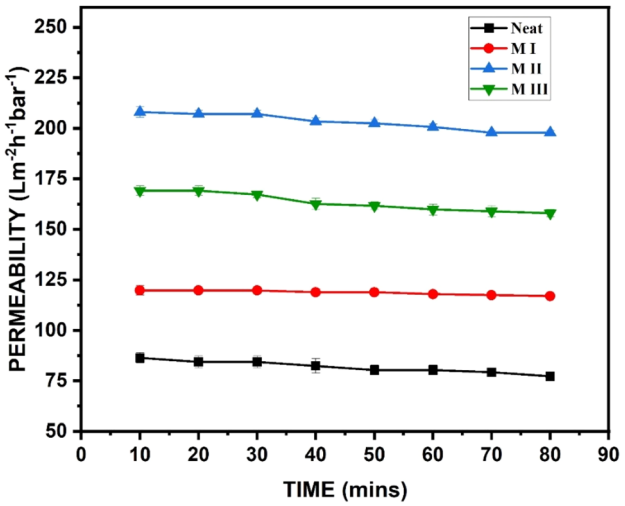

Fig. 13 Pure water permeability of all the fabricated hollow fiber membranes.

was carried out, and the results are presented in Fig. 13. It is observed that the incorporation of the AM–CN composite increases the water permeability by inducing a hydrophilic nature to the membrane. Increasing the dosage of the composite in the membrane matrix, in turn, increased water permeability. However, after a certain amount (*i.e.*, 50 mg), a decline in the water permeability was observed. This decline in permeability may be attributed to the aggregation of the composite during the polymer solution preparation, resulting in a non-uniform dispersion. Additionally, the excess amount of composite might affect the phase inversion process, causing pore blockages or clogging up of the membrane's channels. Pure water permeability study can also be correlated with the contact angle analysis, yielding similar results. In the present study, the neat membrane displayed a pure water permeability of 81.8 L m^{-2} h^{-1} bar^{-1}, whereas the M II membrane displayed the highest pure water permeability of 203.1 L m^{-2} h^{-1} bar^{-1}, making it the optimized membrane.

4.2.6. Antifouling studies. Antifouling studies of the membranes are carried out to evaluate the fouling resistance of the fabricated membranes, as they are susceptible to fouling over time. Fouling is usually caused by the attachment of microbes and pollutants to the membrane surface, leading to the blocking of the pores and channels. However, certain properties such as negative surface charge and enhanced hydrophilicity prevent the firm attachment of the foulants, thereby extending the lifespan and reusability of the membrane.

In the present antifouling study, the membranes are treated with pure water followed by a BSA solution; then, the membranes are washed with water to remove the adsorbed BSA. Finally, the membranes were again treated with pure water. During all these processes, the permeability of the membrane was measured under various feed conditions to estimate different fouling parameters using the equations. Fig. 14 presents the permeability of all the fabricated membranes under different feed conditions.

Among all the fabricated membranes, the neat membrane displayed a flux recovery ratio (FRR) of 42%, whereas the optimized membrane M II displayed an enhanced FRR of 44%. Similarly, the neat membrane exhibited a reversible fouling 'R_r' of 1.4%, and the optimized membrane M II displayed an 'R_r' of 10.7%. This increase of FRR and 'R_r' is mainly due to the influence of the composite, which resulted in a smoother membrane surface, as discussed in AFM analysis. The smooth membrane surface resists the attachment of proteins and, even if any foulants get attached to the surface, they can be easily washed off due to the constant transmembrane pressure acting over the surface, making the membrane less prone to fouling.[39,42] Based on the results of the antifouling studies and Fig. 14, it can be concluded that membrane M II exhibits excellent fouling resistance compared to all the fabricated membranes.

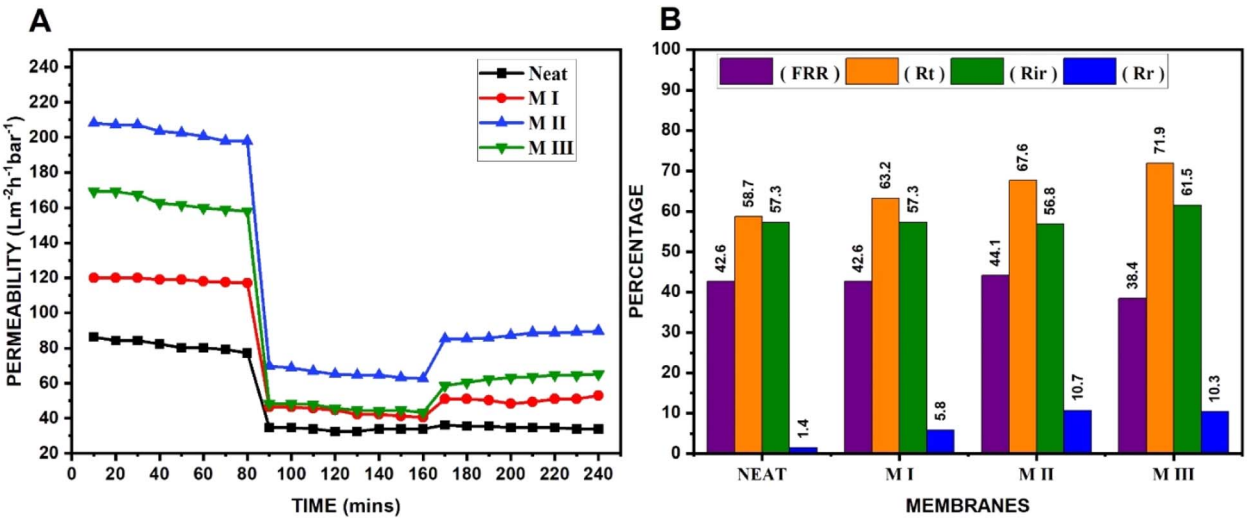

Fig. 14 (A) Permeability during antifouling studies and (B) antifouling parameters of the fabricated membranes.

4.2.7. Dye removal studies. Dye removal capacity of the fabricated membranes was evaluated using 3 different textile dyes, namely Congo red (CR), Reactive Black 5 (RB5), and Reactive Orange 16 (RO16), at different feed concentrations, and their results are presented in Fig. 15. To study the dye removal capacity, both the neat membrane and optimized membrane M II were tested. The M II membrane was selected for this study as it displayed enhanced water permeability and improved antifouling nature among all the fabricated membranes.

For Congo red dye, both the neat membrane and optimized M II membrane displayed rejection above 99% for all the concentrations (*i.e.*, 10, 30, and 50 ppm). Furthermore, a decrease in permeability was observed as the dye concentration increased. Between the two tested membranes, the

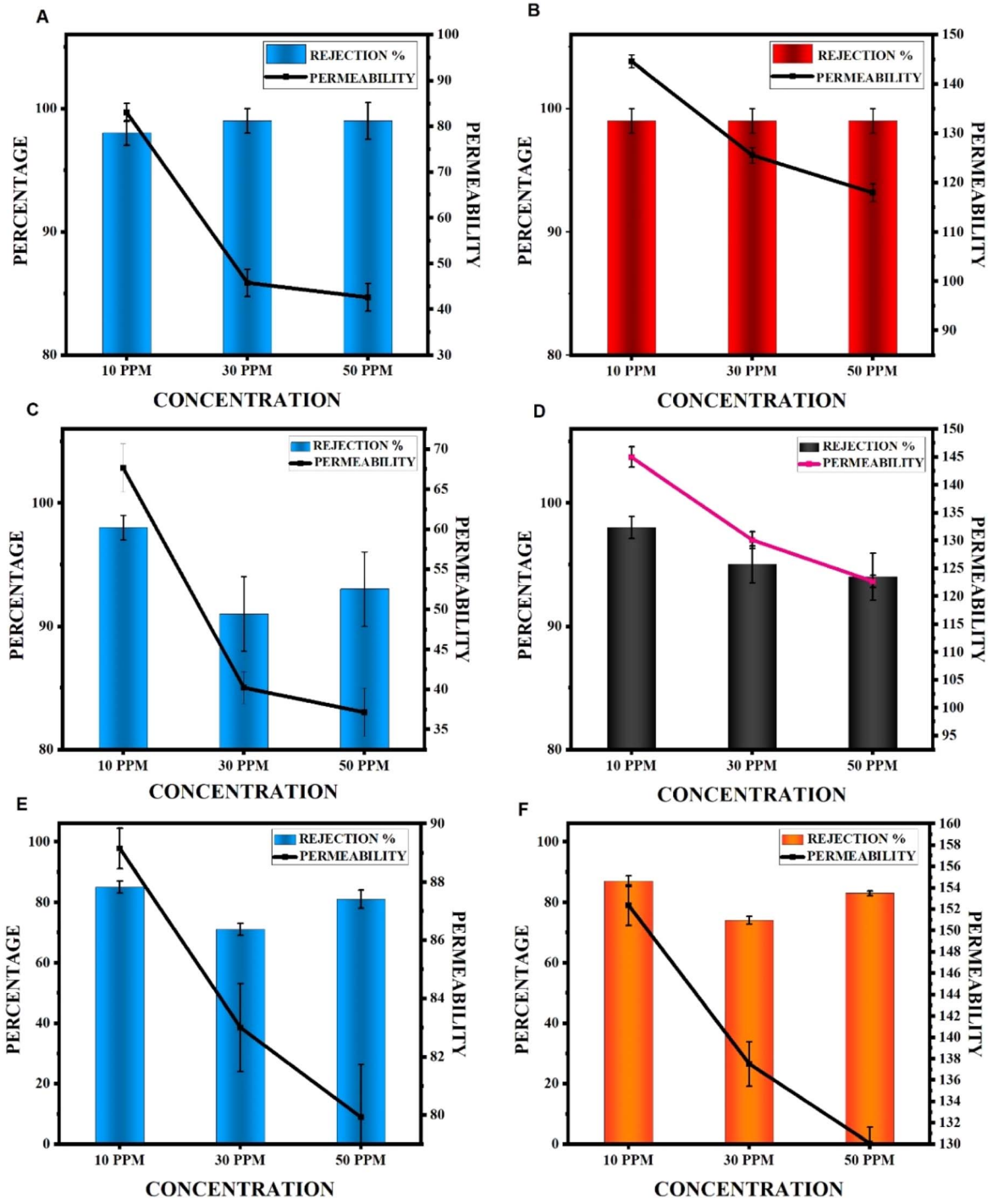

Fig. 15 Rejection and permeability of dye removal studies for neat and M II membranes. Congo red – (A) neat and (B) M II, Reactive black 5 – (C) neat and (D) M II, and Reactive orange 16 – (E) neat and (F) M II.

Table 5 Performance comparison of the fabricated membranes with reported literature[a]

Membrane	Pure water flux (L m^{-1} h^{-1})	Contaminant & removal%	Operating pressure (MPa)	Reference
Polyethyleneimine grafted-polysulfone membrane	150	DY50, EBT & CR – >98%	0.1	43
Polyethyleneimine–polyvinyl chloride	72.7 (per bar)	VBB – >99%	0.3	44
Template-assisted polyetherketone membranes	28.2 (per bar)	CR & CBB – >99%	0.5	45
Lignin/GO integrated polysulfone	247	EY – 81% Lead – >99%	0.2	46
TMA-VBC grafted polysulfone	186.4	VB – 94%	0.1	47
Amyloid/g-C_3N_4 incorporated polysulfone membrane	203 (per bar)	CR – >99% RB5 – 98% RO16 – 88% Lead – 99% Mercury – 75%	0.1	Present work

[a] DY 50 – Direct yellow 50, EBT – Eriochrome black T, CR – Congo red, VBB – Victoria Blue B, CBB – Coomassie brilliant blue, EY – Eosin Y, RO16 – Reactive orange 16, RB5 – Reactive black 5, VB – Victoria Blue, PVDF – polyvinylidene fluoride, TMA – trimethylamine, VBC – 4-vinylbenzyl chlorostyrene, GO – graphene oxide.

optimized M II membrane exhibited higher rejection permeability compared to the neat membrane.

In the case of Reactive black 5 dye and Reactive orange 16 dye, at 10 ppm, the optimized M II membrane demonstrated the highest rejection rate (RB5-98% & RO16-88%), while the neat membrane reported lower rejection rates. As the dye concentration increased, a decrease in the rejection rate was observed. However, for the 50 ppm concentration, the rejection rate was found to be more than 30 ppm. This increase is associated with rapid clogging of the pores, which enhances rejection while simultaneously decreasing permeability. A performance comparison of the present work with a few reported literature studies is presented in Table 5.

4.2.8. Heavy metal removal studies. In the current study, the heavy metal ion removal capacity of the fabricated membrane was tested with the feed solution being a mixture of Pb^{2+} and Hg^{2+} ions in the presence of humic acid. Humic acid was used to mimic groundwater conditions, as it is naturally present in groundwater due to the decomposition of organic matter. It also forms huge complexes with metal ions, making it easier to remove through the filtration process compared to bare metal ions. Fig. 16 displays the heavy metal ion removal capacity of both the neat membrane and optimized membrane M II. Among the two membranes, the M II membranes demonstrated enhanced metal ion rejection of 99% for lead ions and 75% for mercury ions, whereas the neat membrane displayed metal ion rejection of 98% for lead ions and 55% for mercury ions. Along with rejection, the M II membrane also outperformed the neat membrane by exhibiting a higher permeability of 148 L m^{-2} h^{-1} bar^{-1}, with the neat membrane exhibiting a permeability of 106 L m^{-2} h^{-1} bar^{-1}. The higher rejection rate of lead ions can be attributed to their tendency to form large-sized complexes, which are more effectively removed during filtration.[48]

4.2.9. Mechanism of rejection. Rejection or removal of pollutants through membrane-based filtration systems can be predicted through several mechanisms, primarily size exclusion-based removal and interaction-based pollutant removal.

Considering the size exclusion phenomenon through the Structure–Activity Relationship (SAR), RB5 dye exhibits a large complex molecular structure with higher charge density due to the presence of four sulfate groups compared to the other two dyes. These sulfate groups enhance the hydration, thereby increasing effective molecular size and further preventing the dye molecules from passing through the membrane pores.[49] Therefore, RB5 dye exhibits the highest rejection among the three dyes. Between CR and RO16 dyes, CR has a relatively rigid, conjugated molecular structure with stronger charge interactions, leading to a higher rejection than RO16. In contrast, RO16 possesses a more flexible structure due to its single aromatic azo (–N=N–) linkage, which results in lower steric hindrance compared to CR, easing its passage through the membrane.

Although both dyes contain two sulfonate groups, their spatial arrangements are different. In CR, the sulfonate groups are placed far apart on two separate naphthalene moieties, leading to a more extended hydrated structure than RO16. This

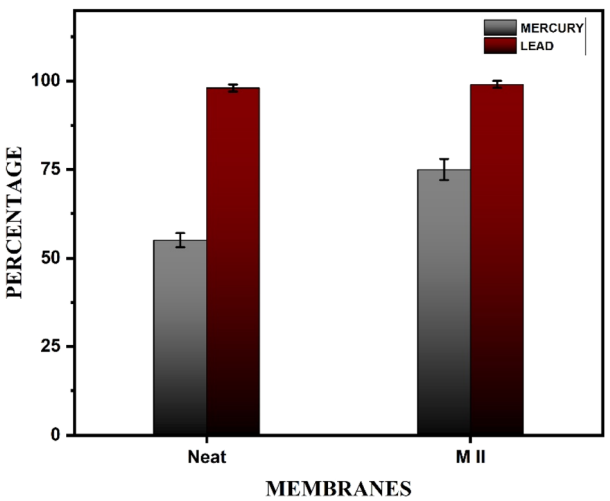

Fig. 16 Heavy metal ion rejection of neat and M II membranes.

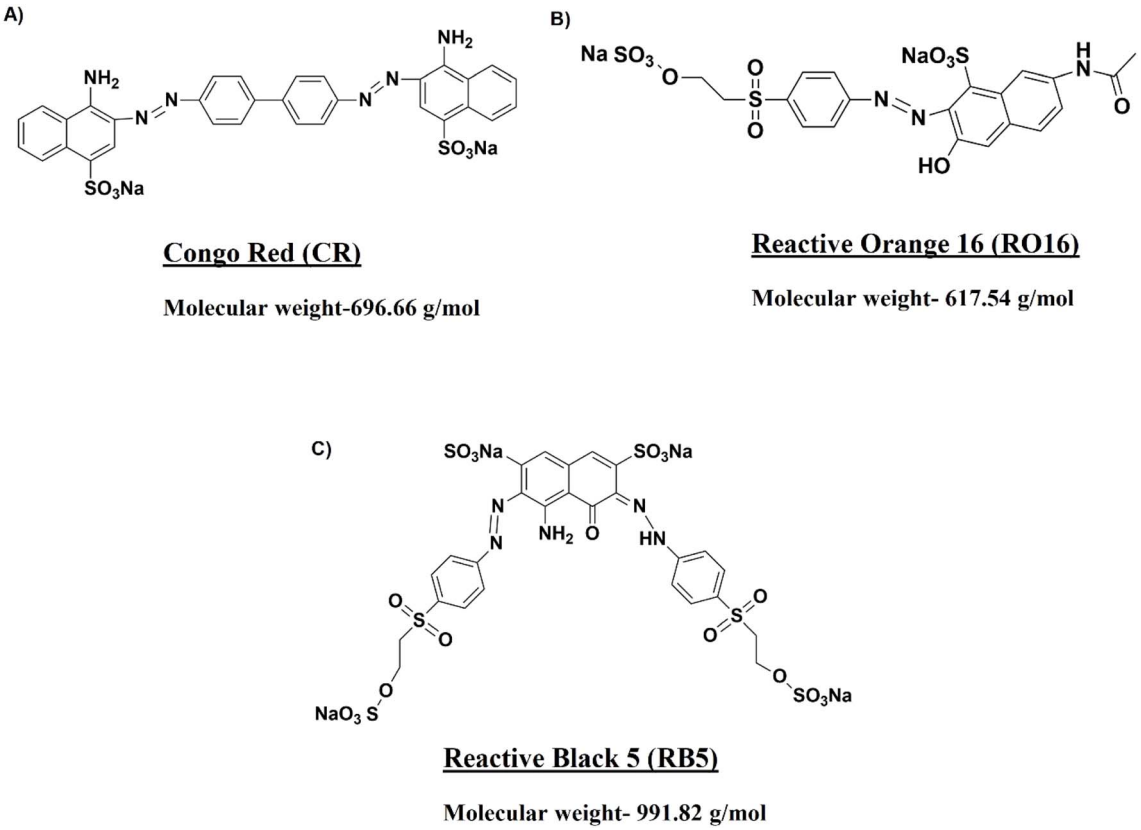

Fig. 17 Structure of the dyes used in the present study: (A) Congo red, (B) Reactive orange 16 and (C) Reactive black 5.

structural characteristic contributes to the higher rejection of CR compared to RO16.[27,50,51] Fig. 17 shows the structures of the dyes used in the experiment.

In the case of heavy metal ion removal, the larger ionic radius and lower charge density of lead ions favor the formation of strong chelating complexes with the carboxyl (–COOH) and hydroxyl (–OH) groups of humic acid, in contrast to mercury ions. These lead–humic acid complexes, due to their larger size, are easily rejected by the membranes. In comparison, mercury ions, with weaker complexation and smaller hydrated size, easily pass through the membrane pores, resulting in lower rejection than lead ions.[27] The metal ion selectivity and binding sites of the metal are discussed in the ESI† through fluorescence and FTIR spectroscopic studies.

In the case of interaction-based phenomena, the composite incorporated in the membrane possesses different functional groups over them, such as an amino group ($-NH_2$), a carboxyl group (–COOH), and a hydroxyl group (–OH). These functional groups act as binding sites for charged dye molecules and metal ions through electrostatic interaction, hydrogen bonding, and forming coordination complexes, thereby sequestering the pollutants from the feed solution.[48,52]

4.2.10. Influence of the functional composite on the membrane structure. The incorporation of the AM–CN composite into the membrane matrix introduces hydrophilic functional groups ($-NH_2$, –COOH, and –OH) that enhance water (non-solvent) influx into the polymer solution during non-solvent-induced phase separation (NIPS). This accelerates the rate of the de-mixing process by reducing the thermodynamic stability of the polymer solution, thereby enhancing membrane porosity. Additionally, the presence of various functional groups on the composite increases the solution's viscosity by interacting with either the polymer or the solvent. The increased viscosity obstructs the outflux of solvent into the nonsolvent, thereby hindering phase separation kinetics and increasing mass transfer resistance. Consequently, this results in the formation of a denser membrane structure.[53]

Altogether, the incorporation of functional composites in the polymer solution enhances thermodynamic factors while simultaneously limiting kinetic factors. Thermodynamic enhancement promotes the development of a porous structure, whereas kinetic resistance favors the formation of a dense membrane morphology. The interplay between these two opposing effects is likely responsible for the optimized membrane (M II) exhibiting a dense skin layer with increased and uniformly distributed porosity.[53–55] As a result, the optimized membrane demonstrates enhanced pure water permeability, higher water uptake, improved porosity, and increased solute rejection compared to the neat polymeric membrane, as discussed in the earlier sections of the present work.

From a structural perspective, both g-C_3N_4 and amyloid proteins are not of crystalline nature but exhibit ordered structures; thus, they are generally regarded as semicrystalline materials. The crystalline fillers are known to impart enhanced

chemical, thermal, and mechanical stability to the membranes along with well-defined morphological structures, which enhance the selectivity. However, these fillers often exhibit poor interfacial compatibility with the polymer solution, leading to aggregation during dope preparation, resulting in membrane defects.[56] In contrast, amorphous fillers generally possess a large number of hydrophilic functional groups, which encourages improved interaction with the dope solution.[57] This enhances the dispersion of the composite in the solution, thereby improving flexibility and water permeability of the membrane. Nonetheless, these amorphous fillers, due to their disordered structure, offer limited mechanical strength and chemical resistance, which may compromise the membrane's longevity.[57] The synthesized composite in the present study is of semi-crystalline nature, which provides a balanced influence of both the crystalline and amorphous regions. The (ordered) crystalline domain provides mechanical robustness, selectivity, and chemical stability, whereas the (disordered) amorphous region contributes to the flexibility and enhanced water permeability of the membrane. This distinct structural duality is responsible for the optimized performance of the membrane.

5. Conclusions and future outlook

In this study, an environment-friendly, economical amyloid–graphitic carbon nitride (AM–CN) composite was synthesized and further verified through FTIR, XRD, zeta potential and TEM imaging. This composite was then incorporated into a polysulfone polymeric solution at varying concentrations to fabricate hollow fiber membranes. Among the fabricated hollow fiber membranes, the neat membrane exhibited a permeability of 81.8 L m^{-2} h^{-1} bar^{-1}, whereas the optimized composite incorporated M II membrane displayed a significantly higher permeability of 203.1 L m^{-2} h^{-1} bar^{-1}. Additionally, the M II membrane also displayed enhanced antifouling behavior with reversible fouling of 10.7% and a flux rejection ratio of 44%. The optimized M II membrane also exhibited excellent dye rejection capacity of >99% for Congo red, >98% for Reactive black 5, and 88% for RO16 dye. Furthermore, in heavy metal ion removal, the membrane also displayed a rejection of 99% for Pb^{2+} and 75% for Hg^{2+} ions in a humic acid complexed state, simulating groundwater conditions. Despite these remarkable results, further studies are required to evaluate the rejection capacity for a broader range of textile dyes. For the future outlook, the rejection of different heavy metal ions needs to be explored in the ionic state of metals. The fabrication of thin film composite membranes using the AM–CN composite may further enhance heavy metal ion removal and extend the potential application of this material for advanced water purification technologies.

Data availability

The datasets generated and/or analyzed are available from the corresponding author upon reasonable request. All relevant characterization data (SEM, FTIR, XRD, UV-vis, TGA, *etc.*) that support the findings of this study have been included in the manuscript and the ESI.†

Conflicts of interest

There are no conflicts to declare.

Acknowledgements

The authors are grateful to the National Institute of Technology Karnataka (NITK), Surathkal, India, for providing laboratory and instrumentation facilities. We are also thankful to the Central Research Facility (CRF), NITK, for hollow fiber spinning and characterization facilities, Central Innovation Facility (CIF) Manipal Institute of Technology, and Materials Research Centre, MNIT Jaipur, for characterization facilities. The authors are also thankful to VGST, Department of IT, BT and ST, Government of Karnataka, India.

References

1 A. K. Roy Choudhury, in *Roadmap to Sustainable Textiles and Clothing: Environmental and Social Aspects of Textiles and Clothing Supply Chain*, ed. S. S. Muthu, Springer, Singapore, 2014, pp. 1–39.
2 U. Kumari, in *Dye Pollution from Textile Industry: Challenges and Opportunities for Sustainable Development*, ed. P. Singh, Springer Nature, Singapore, 2024, pp. 17–30.
3 S. Sinha, N. Jahan and P. R. Agrawal, in *Dye Pollution from Textile Industry: Challenges and Opportunities for Sustainable Development*, ed. P. Singh, Springer Nature, Singapore, 2024, pp. 31–63.
4 A. S. Mohammed, A. Kapri and R. Goel, in *Biomanagement of Metal-Contaminated Soils*, ed. M. S. Khan, A. Zaidi, R. Goel and J. Musarrat, Springer Netherlands, Dordrecht, 2011, pp. 1–28.
5 A. H. Jagaba, I. M. Lawal, A. H. Birniwa, A. C. Affam, A. K. Usman, U. B. Soja, D. Saleh, A. Hussaini, A. Noor and N. S. A. Yaro, in *Membrane Technologies for Heavy Metal Removal from Water*, CRC Press, 2024.
6 S. Khan and A. Malik, in *Environmental Deterioration and Human Health: Natural and Anthropogenic Determinants*, ed. A. Malik, E. Grohmann and R. Akhtar, Springer Netherlands, Dordrecht, 2014, pp. 55–71.
7 M. Zaynab, R. Al-Yahyai, A. Ameen, Y. Sharif, L. Ali, M. Fatima, K. A. Khan and S. Li, *J. King Saud Univ., Sci.*, 2022, **34**, 101653.
8 A. G. (Tony) Fane, R. Wang and Y. Jia, in *Membrane and Desalination Technologies*, ed. L. K. Wang, J. P. Chen, Y.-T. Hung and N. K. Shammas, Humana Press, Totowa, NJ, 2011, pp. 1–45.
9 M. M. Pendergast and E. M. V. Hoek, *Energy Environ. Sci.*, 2011, **4**, 1946–1971.
10 A. G. Fane, R. Wang and M. X. Hu, *Angew. Chem., Int. Ed.*, 2015, **54**, 3368–3386.
11 N. Peng, N. Widjojo, P. Sukitpaneenit, M. M. Teoh, G. G. Lipscomb, T.-S. Chung and J.-Y. Lai, *Prog. Polym. Sci.*, 2012, **37**, 1401–1424.
12 C. Y. Feng, K. C. Khulbe, T. Matsuura and A. F. Ismail, *Sep. Purif. Technol.*, 2013, **111**, 43–71.

13 M. Mondal, M. Dutta and S. De, *Sep. Purif. Technol.*, 2017, **188**, 155–166.
14 D. Qadir, H. Mukhtar and L. K. Keong, *Sep. Purif. Rev.*, 2017, **46**, 62–80.
15 B. M. Ganesh, A. M. Isloor and A. F. Ismail, *Desalination*, 2013, **313**, 199–207.
16 P. Wan, Z. Zhang and B. Deng, *Ind. Eng. Chem. Res.*, 2019, **58**, 3339–3348.
17 N. Prabhakar, A. M. Isloor, M. Padaki and A. Fauzi Ismail, *Chem. Eng. J.*, 2024, **498**, 155270.
18 F. Yang, Z. Yan, J. Zhao, S. Miao, D. Wang and P. Yang, *J. Mater. Chem. A*, 2020, **8**, 3438–3449.
19 H. Ye, C. Liu, M.-B. Wu, L.-L. Ma, S.-C. Liu, Y. Zhong and J. Yao, *J. Mater. Chem. A*, 2022, **10**, 2987–2994.
20 S. Bolisetty and R. Mezzenga, *Nat. Nanotechnol.*, 2016, **11**, 365–371.
21 S. Bolisetty, N. M. Coray, A. Palika, G. A. Prenosil and R. Mezzenga, *Environ. Sci.:Water Res. Technol.*, 2020, **6**, 3249–3254.
22 T. Jin, M. Peydayesh, H. Joerss, J. Zhou, S. Bolisetty and R. Mezzenga, *Environ. Sci.:Water Res. Technol.*, 2021, **7**, 1873–1884.
23 M. Peydayesh, M. K. Suter, S. Bolisetty, S. Boulos, S. Handschin, L. Nyström and R. Mezzenga, *Adv. Mater.*, 2020, **32**, 1907932.
24 D.-D. Yang, F.-X. Chang, B.-F. Zhang and Y.-C. Yong, *Bioresources and Bioprocessing*, 2024, **11**, 22.
25 Y. Li, M.-Q. Wang, S.-J. Bao, S. Lu, M. Xu, D. Long and S. Pu, *Ceram. Int.*, 2016, **42**, 18521–18528.
26 P. Bharmoria, D. Mondal, M. M. Pereira, M. C. Neves, M. R. Almeida, M. C. Gomes, J. F. Mano, I. Bdikin, R. A. S. Ferreira, J. A. P. Coutinho and M. G. Freire, *Commun. Mater.*, 2020, **1**, 1–13.
27 G. P. Syed Ibrahim, A. M. Isloor, A. F. Ismail and R. Farnood, *Sci. Rep.*, 2020, **10**, 6880.
28 J. A. Prince, S. Bhuvana, K. V. K. Boodhoo, V. Anbharasi and G. Singh, *J. Membr. Sci.*, 2014, **454**, 538–548.
29 R. S. Hebbar, A. M. Isloor, K. Ananda and A. F. Ismail, *J. Mater. Chem. A*, 2016, **4**, 764–774.
30 G. P. S. Ibrahim, A. M. Isloor, A. Moslehyani and A. F. Ismail, *J. Water Proc. Eng.*, 2017, **20**, 138–148.
31 R. S. Hebbar, A. M. Isloor, K. Ananda, M. Sohaimi Abdullah and A. F. Ismail, *New J. Chem.*, 2017, **41**, 4197–4211.
32 P. Satishkumar, A. M. Isloor, L. N. Rao and R. Farnood, *ACS Omega*, 2024, **9**, 25766–25778.
33 G. K. Gbassi, F. S. Yolou, S. O. Sarr, P. G. Atheba, C. N. Amin and M. Ake, *Int. J. Biol. Chem. Sci.*, 2012, **6**, 1828–1837.
34 R. Wang and Y. Wang, *Int. J. Mol. Sci.*, 2021, **22**, 1206.
35 P. Qiu, H. Chen, C. Xu, N. Zhou, F. Jiang, X. Wang and Y. Fu, *J. Mater. Chem. A*, 2015, **3**, 24237–24244.
36 K. L. Morris and L. C. Serpell, in *Amyloid Proteins: Methods and Protocols*, ed. E. M. Sigurdsson, M. Calero and M. Gasset, Humana Press, Totowa, NJ, 2012, pp. 121–135.
37 R. S. Harrison, P. C. Sharpe, Y. Singh and D. P. Fairlie, in *Reviews of Physiology, Biochemistry and Pharmacology*, ed. S. G. Amara, E. Bamberg, B. Fleischmann, T. Gudermann, S. C. Hebert, R. Jahn, W. J. Lederer, R. Lill, A. Miyajima, S. Offermanns and R. Zechner, Springer, Berlin, Heidelberg, 2007, pp. 1–77.
38 D. Kadadou, T. Arumugham, L. Tizani and S. W. Hasan, *npj Clean Water*, 2024, **7**, 1–11.
39 M. Elimelech, X. Zhu, A. E. Childress and S. Hong, *J. Membr. Sci.*, 1997, **127**, 101–109.
40 K.-Y. Law, *J. Phys. Chem. Lett.*, 2014, **5**, 686–688.
41 L. H. T. Lyly, B. S. Ooi, J. K. Lim, C. J. C. Derek and S. C. Low, *J. Environ. Chem. Eng.*, 2021, **9**, 104627.
42 L. Liu, Y. Liu, X. Chen, S. Feng, Y. Wan, H. Lu and J. Luo, *J. Membr. Sci.*, 2023, **668**, 121205.
43 P. Ge, Z. Lin, J. Yang, C. Hu, Q. Liu and Q. Zhang, *J. Membr. Sci.*, 2023, **672**, 121428.
44 K. Ren, X. Lu, S. Zheng, H. Zhang and J. Gu, *J. Hazard. Mater.*, 2024, **475**, 134856.
45 Y. Huang, G. Zhang, X. Zhang, J. Shu, C. Wang, Z. Zhai, X. Jie, S. Zhao and Y. Zhao, *J. Membr. Sci.*, 2024, **698**, 122634.
46 S. Dhara, A. D. Sontakke, N. Shekhar Samanta, R. Venkata Sai Uppaluri and M. K. Purkait, *Sep. Purif. Technol.*, 2024, **341**, 126894.
47 H. Wu, T. Hao, X. Liu, Y. Lin, D. Sun, L. Wang, Y. Tian, H. Yao, H. Xie, J. Zhang, L. Yu, Z. Yang, H. Wang and X. Wang, *Sep. Purif. Technol.*, 2025, **367**, 132806.
48 R. S. Hebbar, A. M. Isloor, B. Prabhu, Inamuddin, A. M. Asiri and A. F. Ismail, *Sci. Rep.*, 2018, **8**, 4665.
49 J. Lin, W. Ye, H. Zeng, H. Yang, J. Shen, S. Darvishmanesh, P. Luis, A. Sotto and B. Van der Bruggen, *J. Membr. Sci.*, 2015, **477**, 183–193.
50 J. Lin, W. Ye, M.-C. Baltaru, Y. P. Tang, N. J. Bernstein, P. Gao, S. Balta, M. Vlad, A. Volodin, A. Sotto, P. Luis, A. L. Zydney and B. Van der Bruggen, *J. Membr. Sci.*, 2016, **514**, 217–228.
51 R. Ahmad, J. Guo and J. Kim, *J. Cleaner Prod.*, 2019, **232**, 608–616.
52 R. S. Hebbar, A. M. Isloor, A. K. Zulhairun, M. Sohaimi Abdullah and A. F. Ismail, *J. Taiwan Inst. Chem. Eng.*, 2017, **72**, 244–252.
53 M. Sadrzadeh and S. Bhattacharjee, *J. Membr. Sci.*, 2013, **441**, 31–44.
54 M. Yousefian-Arani, A. Sharif and M. Karimi, *J. Mol. Liq.*, 2022, **362**, 119732.
55 T. Ahmad, L. M. Rehman, R. Al-Nuaimi, J.-P. B. B. de Levay, R. Thankamony, M. Mubashir and Z. Lai, *Chemosphere*, 2023, **337**, 139430.
56 S. Yu, C. Li, S. Zhao, M. Chai, J. Hou and R. Lin, *Nanoscale*, 2024, **16**, 7716–7733.
57 M. Carta, A. R. Antonangelo, J. C. Jansen and M. Longo, *Polymers*, 2023, **15**, 2951.

